



A microwave resonator integrated on a polymer microfluidic chip



S.Z. Kiss^{a,*}, A.M. Rostas^b, L. Heidinger^b, N. Spengler^a, M.V. Meissner^a, N. MacKinnon^a, E. Schleicher^b, S. Weber^b, J.G. Korvink^{a,*}

^a Institute of Microstructure Technology (IMT), Karlsruhe Institute of Technology, Hermann-von-Helmholtz-Platz 1, 76344 Eggenstein-Leopoldshafen, Germany

^b Institute of Physical Chemistry (IPC), University of Freiburg, Albertstr. 21, 79104 Freiburg, Germany

ARTICLE INFO

Article history:

Received 9 June 2016

Revised 16 July 2016

Accepted 18 July 2016

Available online 19 July 2016

Keywords:

EPR

ESR

Resonator

Stacked resonator

Resonator modes

Small-volume EPR

Microfluidic

Fluidic chip

Spin nutation

Transient EPR

ABSTRACT

We describe a novel stacked split-ring type microwave (MW) resonator that is integrated into a 10 mm by 10 mm sized microfluidic chip. A straightforward and scalable batch fabrication process renders the chip suitable for single-use applications. The resonator volume can be conveniently loaded with liquid sample via microfluidic channels patterned into the mid layer of the chip. The proposed MW resonator offers an alternative solution for compact in-field measurements, such as low-field magnetic resonance (MR) experiments requiring convenient sample exchange. A microstrip line was used to inductively couple MWs into the resonator. We characterised the proposed resonator topology by electromagnetic (EM) field simulations, a field perturbation method, as well as by return loss measurements. Electron paramagnetic resonance (EPR) spectra at X-band frequencies were recorded, revealing an electron-spin sensitivity of $3.7 \cdot 10^{11}$ spins \cdot Hz^{-1/2} G⁻¹ for a single EPR transition. Preliminary time-resolved EPR experiments on light-induced triplet states in pentacene were performed to estimate the MW conversion efficiency of the resonator.

© 2016 Published by Elsevier Inc.

1. Introduction

For EPR spectroscopy, a MW resonant structure is a key component of the experimental setup. At resonance, it concentrates the magnetic field in a confined spatial region, increasing the typically weak spin-to-field interaction significantly. Consequently, resonator topologies that efficiently convert MW power P into an oscillating magnetic field $B_1 = 2B_1^r \cos(\omega t)$ of high-magnitude B_1^r and minimize heating of the sample due to the electric component of the MW, are desirable to achieve a high enough sensitivity (minimum number of detectable spins). This resonator characteristic is described by the MW conversion efficiency $\Lambda = B_1^r/P^{1/2}$. Loss mechanisms that compromise the resonator's performance should be minimised, demanding a high quality factor Q . Maximising the filling factor $\eta \approx V_s/V_r$, i.e., the volume fraction of paramagnetic sample in the sensitive area of the resonator, is particularly essential for experiments on precious samples available only in small quantities.

In recent years, several authors have applied this rationale to achieve inductively detected EPR of volume-limited samples using miniaturised surface resonators [1–10]. Narkowicz et al. [11] employed planar microresonators (PMRs) based on a microstrip line topology featuring loop diameters D of down to 20 μ m, designed for operation at 14 GHz. The authors demonstrated that the MW efficiency factor Λ and sensitivity scale with the PMRs diameter as $D^{-(0.8...1)}$ [11]. EPR resonators based on transmission lines, such as compact striplines [12] and microstrip lines [13,14] have been investigated to increase sensitivity of the EPR experiment. Twig et al. [15] proposed surface loop-gap microresonators with inner dimensions ranging from 150 μ m down to 2 μ m for operation at the Ku, Q, and W frequency bands.

All of these studies take advantage of the convenient scalability offered by surface micromachining, and compensate the typically low quality factors (on the order of 100 compared to, e.g., metal cavities with Q 's up to several 1000s) of microresonators by their inherently high filling factors. Indeed, the low Q factor of a surface resonator is a major advantage for pulse EPR experiments [11,12] operating at considerably reduced MW input power, in which broad bandwidths and a short dead-time after excitation are required. However, the operation of miniaturised resonators involve several issues: (i) Sample handling, including the exact

* Corresponding authors at: Institute of Microstructure Technology (IMT), Karlsruhe Institute of Technology, Hermann-von-Helmholtz-Platz 1, 76344 Eggenstein-Leopoldshafen, Germany.

E-mail address: sebastian.kiss@kit.edu (S.Z. Kiss).

URL: <http://www.imt.kit.edu> (S.Z. Kiss).

positioning of the sample into the resonator, becomes increasingly difficult; (ii) The sample proximity to the metal walls of the resonator may cause static magnetic field distortions due to susceptibility mismatch; (iii) The MW magnetic field magnitude rapidly decays and/or is typically inhomogeneous throughout the sample region; and (iv) The electric field can leak into the sample region causing severe dielectric heating.

In this work we present a novel stacked split-ring [16–18] type MW resonator fabricated by means of surface micromachining techniques, in order to address the aforementioned problems. In our design we implement fluidic channels, as known from Lab-on-a-chip devices, that can easily handle sub-microliter volumes and precisely position the sample in the active region of the resonator. The sample reservoir, as well as the channels, are defined by a polymer layer which is sandwiched in between two polyimide films that together feature a resonator structure. Therefore, the sample is always separated and electrically isolated from any metal parts. Liquid samples can be remotely introduced into the resonator, e.g., via tubings driven by a syringe pump. The stacked ring topology, as well as the interdigitated design of the proposed resonator, are designed to offer both a homogeneous magnetic field distribution of high magnitude, and a minimal exposure of sample to the electric field.

2. Design and simulation

2.1. Design

A diagram detailing our probehead is shown in Fig. 1. It consists of two key parts, (i) the MW resonator implemented on a polymer chip and featuring a microfluidic sample channel and (ii) a microstrip line MW coupling structure. Fig. 1(a) presents a schematic of the basic model parameters that are also summarised in Table 1.

The proposed MW resonator is a stacked double split-ring type structure. Copper rings are formed on the top and bottom face of the $(10 \times 10 \times 0.65) \text{ mm}^3$ ($w \times l \times h$) small chip. The inner and outer ring radius r_i and r_o as denoted in Fig. 1(a) are related by the fixed ratio $r_o = 3r_i$. We designed the split region such that inter-digitating fingers, separated by a distance g_c , form

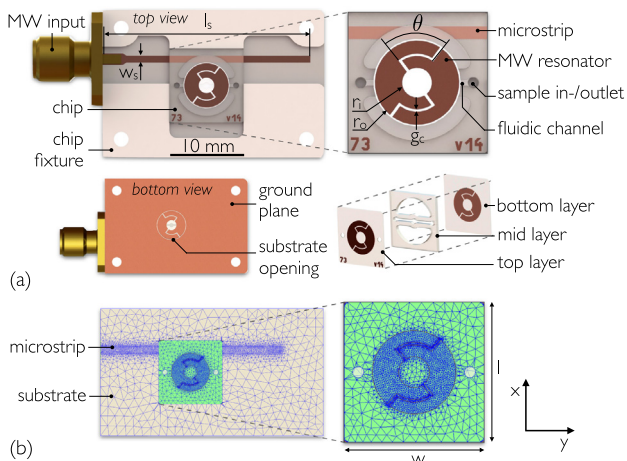


Fig. 1. (a) Schematic representation of the microstrip line coupling structure (top and bottom view) as well as the three-layer-stack resonator chip. The fixture for the chip and the substrate are made from the same material (see Section 3 for details). Denoted are the principle design variables used to define the geometry. The operation frequency of the resonator is mainly determined by its outer radius r_o , which was kept constant for this study, and the design variable θ . The mid layer of the chip features the fluidic channels, which could accommodate additional fluidic unit operations, e.g., analyte separation or mixing. (b) Detail of the refined tetrahedral mesh of the computational model as used for FEM simulation.

Table 1

Design variables and representative values as used to simulate the EM field profiles of Figs. 2 and 3. The variable i_h denotes the chip's height.

l_s (mm)	w_s (mm)	r_o (mm)	r_i (mm)	g_c (mm)	i_h (mm)	θ ($^\circ$)
28	0.9	3	1	0.15	0.65	80

distributed capacitors. Another capacitive pathway is present between the overlapping metalization area from the two copper ring tracks separated by the chip, which acts as a dielectric. The resonance of the structure is primarily determined by the outer-ring radius r_o , the top/bottom ring separation distance (i.e., the insert height i_h), the geometry of the finger, and the distance between the microstrip line and the resonator. The opening angle of the finger θ , as depicted in Fig. 1(a), is a design variable used to adjust the resonator's resonance frequency without changing its outer diameter. The chip is easily filled with sample solution, and fluidic channels guide the fluid to a reservoir of approximately $1 \mu\text{L}$ active volume.

An open-ended microstrip line of length l_s is used to excite the resonator. The electrical length is chosen to match $(3/2)\lambda$ at 9.5 GHz, resulting in a magnetic field maximum at the centre of the microstrip transmission line. This allows for efficient inductive side-coupling of MW energy into the resonator positioned at a distance of $(3/4)\lambda$ from the open end of the microstrip line. Substrate and ground-plane material from beneath the MW resonator is removed by a through-hole ($100 \mu\text{m}$ larger than r_o) to reduce constraints on the resonator's EM characteristic. The microstrip line is designed to have a characteristic impedance Z_0 of 50Ω , by adjusting its track width w according to known formulas [19]. The skin depth in copper at 9.5 GHz is around $1 \mu\text{m}$, thus well below the employed copper thickness of $35 \mu\text{m}$ for the microstrip line and $9 \mu\text{m}$ for the resonator. The input port of the microstrip line is soldered to an SMA flange connector that connects via a semi-rigid coaxial cable (CE50047, Elspec GmbH, Germany) to the EPR MW-bridge.

2.2. Simulation

To gain more detailed insight into the EM behaviour, the structure was simulated using the finite element method (FEM) software HFSS (ANSYS, version 16), to extract the EM field distributions and resonance frequencies f_i . The model included the microstrip line coupling structure on 0.46 mm thick high frequency laminate, and the MW resonator made from $9 \mu\text{m}$ copper on polyimide sheets. For our studies we kept the outer radius r_o of the resonator constant at $r_o = 3 \text{ mm}$. For the frequency sweep analysis, a wave port of 50Ω impedance was used for continuous (CW) MW excitation, and was defined directly on the front facet of the microstrip transmission line. The simulation model included loss effects for the materials used (Rogers RO4003C substrate, polyimide and copper). The whole structure was placed inside a box-shaped domain to model the surrounding air. Back scattering was avoided by applying a radiation boundary condition, which acted as an absorbing layer. As shown in Fig. 1(b), the free tetrahedral mesh was refined to resolve the structure accurately, e.g., for small geometry features such as the interdigitated fingers of the resonator. Model parameters were systematically changed until the reflected power was minimal, indicating a matched impedance between resonator and the distributed coupling circuit.

Fig. 2 visualises the electric and magnetic field distribution of the resonator within the x/y -plane of the chip. The first four resonator modes computed from an eigenmode analysis are shown. The EM field distribution of the resonator is important for our application. A strong static magnetic field B_0 , e.g., along the x -axis, causes a net magnetisation of the sample. The resonator's

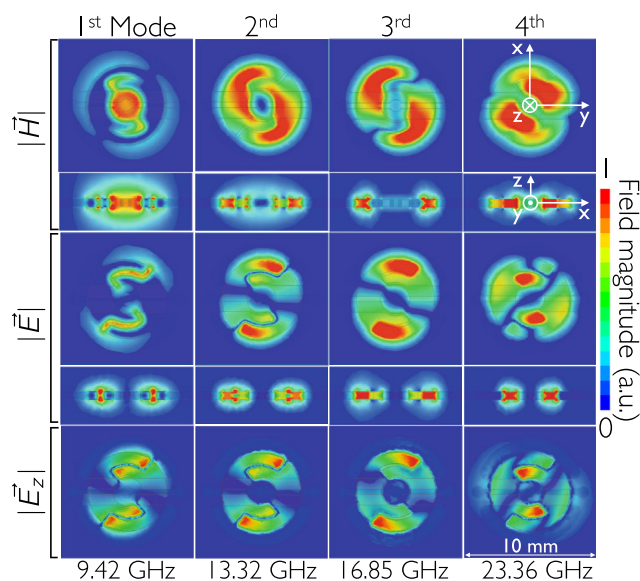


Fig. 2. Eigenmode simulation of an unloaded MW resonator with a targeted operating frequency of 9.5 GHz. Shown are the qualitative electric and magnetic field distributions of the first four eigenmodes. The first four rows show the field magnitudes plotted on the symmetry cut plane at half height of the chip and the corresponding z/x -cross section. The bottom row shows the magnitude of the z -component of the electric field plotted 300 μm above the resonators surface. The fundamental mode localises the magnetic field maximum within the resonator centre, coinciding with the sample reservoir. The electric field is localised between the interdigitating fingers and only minimally overlaps with the sample region.

oscillating magnetic field B_1 , when orthogonal to B_0 (e.g., along the z -axis), excites the spin species present in the sample in resonance with its corresponding precession frequency. The spin relaxation and MW transmitter power absorption processes are then amenable to measurements.

EPR experiments require resonators to efficiently generate high magnetic fields within the sample volume under investigation. At the same time, the electric field magnitude E_1 impinging the sam-

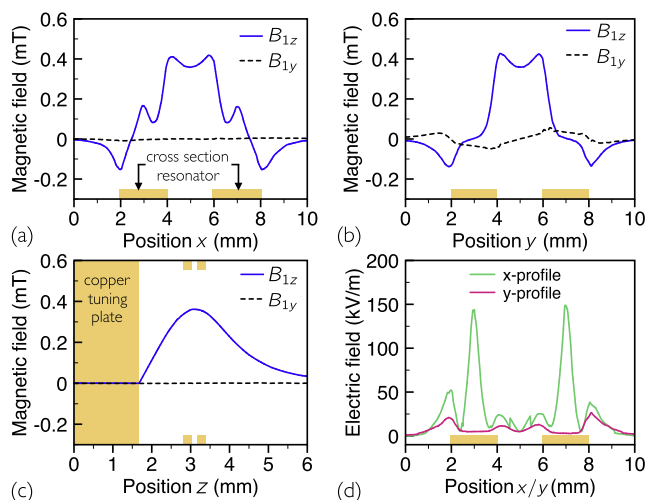


Fig. 3. Field profiles extracted from the simulation study (MW input power $P = 1$ W). (a) and (b) Magnetic field components B_{1z} and B_{1y} as a function of x and y , i.e., in the cutting plane at half the height of the chip, (c) B_{1z} in the resonator's axial direction, perpendicular to its surface. A copper plate introduced from above for frequency tuning perturbs the otherwise symmetric field profile. Dashed lines represent the in-plane magnetic field component B_{1y} with negligible magnetic field contribution. (d) Electric field magnitude plotted as a function of x and y . Electric and magnetic field maxima are well separated.

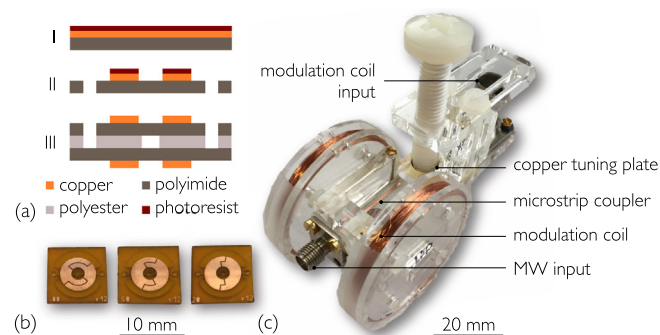


Fig. 4. (a) Process flow-chart for resonator chip fabrication. The compound step II included laser ablation of photoresist as well as laser cutting of the alignment holes, followed by chemical wet etching of copper. (b) Representative 10 by 10 mm chips featuring MW resonators of different θ values. (c) Fabricated fixture made from PMMA including the MW resonator, a copper plate for frequency tuning as well as custom made EPR modulation coils.

ple should be maintained as low as possible to minimize dielectric sample heating. Polar and electrically conductive sample solutions, in particular, easily absorb MW power P_{abs} that scales as $P_{\text{abs}} \propto \epsilon |E_1|^2$, with ϵ being the sample permittivity, and can cause significant increases in temperature. We therefore consider the fundamental mode of the resonator (left column in Fig. 2) which fulfills the aforementioned requirements.

We analysed the results from the simulation, using the parameters as displayed in Table 1, more closely. Fig. 3(a)–(c) summarises the findings quantitatively. At positions where the sample is located (centre of resonator, position $x = y = 5$ mm), the MW magnetic field B_{1z} had its maximum strength as would be desired for spin excitation in EPR experiments. Dashed lines represent the transverse magnetic field component B_{1y} perpendicular to the resonator axis showing only a negligible contribution to the main MW field excitation along the z -axis. The profile of the unperturbed magnetic field's z -component B_{1z} in the z -direction is perfectly symmetric about the x -axis, has its maximum at the half height of the insert, and decays rapidly outside of this region. For the simulated case shown in Fig. 3(c) a thin copper plate for frequency tuning was in place, braking the symmetry. The z -component of the MW magnetic field profile along the x/y -axis shows a dip at the centre of the resonator, leading to a 17% decrease in magnetic flux density compared to the average value of 0.39 mT considered within $2r_1$. The MW conversion factor is computed from the average B_{1z} field values across the inner ring diameter to be approximately $A_{\text{cal}} = 0.39 \text{ mT W}^{-1/2}$.

3. Fabrication

The chips featuring the MW resonator were fabricated from three layers of polymer that were cut and structured with a UV laser (TruMark 6330, Trumpf, Germany). The copper resonators were defined by chemical wet etching. Top and bottom sheets (AkaFlex KCL 2-9/26 HT, Krempel GmbH) of the insert were made from 25 μm thick polyimide sheets with a single-sided laminated layer of 9 μm thick copper. Fig. 4(a) outlines the basic process flow in three steps.

For step I the polyimide sheets were cut and glued to a 4 inch handling wafer, spincoated for 60 s at 3000 rpm with 2 μm thick AZ4015 photoresist (MicroChemicals GmbH, Germany). UV laser machining was employed for both maskless ablation of the photoresist, to define the resonator pattern, as well as for cutting the polymer sheets to define the individual chips. A prior cleaning step of the copper surface by a 10 s dip in sodium persulfate ($\text{Na}_2\text{S}_2\text{O}_8$,

250 g per 1 L) solution enhanced photoresist adhesion. Microfluidic inlet and outlet ports, as well as alignment holes, were subsequently also laser-cut. Exposed copper parts were removed by wet-etching for approximately 5 min in a sodium persulfate solution (Fig. 4(a) step II). Etched structures showed geometric conformity with a relative deviation of less than 1%. The process allows minimal feature sizes of down to 40 μm without significant artefacts due to, e.g., over-etching. After etching, the photoresist was stripped and the polyimide sheets were removed from the handling wafer. The mid layer featuring the sample reservoir was cut out of two stacked sheets, double-liner adhesive sheets (7961MP, 3M, $\epsilon_r = 3.42$, $\tan \delta = 0.01$) using the same UV laser. The sheets are constructed from a double coated 0.18 mm thick polyester carrier featuring 0.05 mm adhesive layers (200MP, 3M, High Performance Acrylic Adhesive). After cutting, the protective paper was removed and the processed top and bottom polyimide sheets were aligned to the reservoir layer by using alignment pins. The assembled stack was laminated under heat by a hot roll laminator (LP25HS, ACCO Rexel). Alignment marks enabled precise laser cutting of the laminated stack into single chips shown in Fig. 4(b).

The microstrip line coupling structure was defined by precision milling (ICV 4030, isel, Germany) of the top copper layer (35 μm thickness) of a 0.406 mm thick high frequency laminate (Rogers RO4003C, $\epsilon_r = 3.55$, $\tan \delta|_{f=10\text{GHz}} = 0.0027$). The coupling structure was mounted on a custom made holder laser cut (VLS2.30, Universal Laser Systems Inc.) from polymethyl methacrylate (PMMA) sheets. The fabricated holder shown in Fig. 4(c) is equipped with a set of EPR modulation coils of 40 mm in outer diameter featuring 150 windings each wound from isolated copper wire (100 μm in outer diameter). A proprietary coaxial connector (Bruker) was employed to connect the coils to the modulation coil driver of the EPR spectrometer.

4. Experimental performance

4.1. Resonator characterisation

All radio frequency (RF) measurements were performed using the fixture shown in Fig. 4(c), without the modulation coil in place. The resonator chips were mounted and operated in the orientation as shown in Fig. 1(b). Resonance frequencies f_i and loaded quality

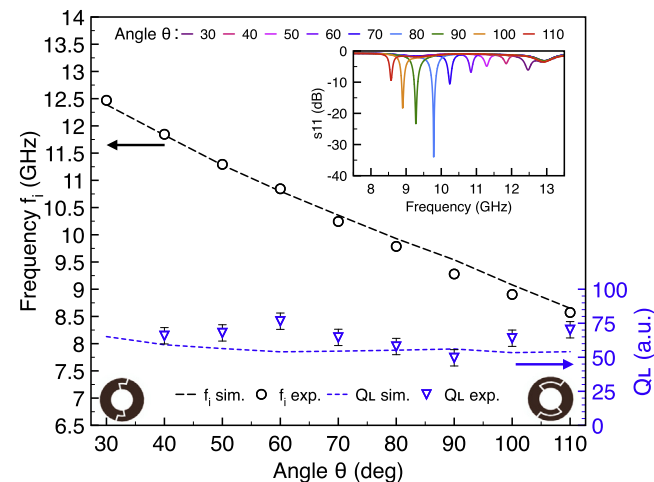


Fig. 5. Measured (solid lines) and simulated (dashed lines) resonance frequencies f_i and loaded quality factors Q_L as a function of the design variable θ ; each data point represents a separate resonator. The inset shows the measured spectra of the reflection coefficient S_{11} . Arrows indicate the corresponding axis for the plotted data.

factors $Q_L = f_0/(f_2 - f_1)$, as shown in Fig. 5, were determined from power reflection curves measured by a calibrated network analyser (ZVA24, Rohde & Schwarz, Germany).

Acquired S-parameter data were averaged ten times, and base-lines were corrected by a linear fit, to accurately determine the -3 dB frequencies f_1 and f_2 at each side of the resonance. For tuning the resonance frequency, a circular copper sheet co-axially aligned with the resonator was attached to the blunt tip of a polymer screw which enabled continuous adjustment of the tuning distance. Fig. 6(a) illustrates the strong dependency of f_0 on the tuning position. The frequency tuning curve as shown in Fig. 6(a) was measured from an unloaded resonator with an outer radius r_o of 3 mm and a value for θ of 53° . Table 2 summarises the measured results for three distances between the copper sheet and the resonator surface. Coupling factors κ of the tuned resonators were determined from the Smith chart shown in Fig. 6(b) in order to evaluate their unloaded quality factor $Q_0 = Q_L(1 + \kappa)$.

The EM field distribution of the resonator was experimentally evaluated by means of a perturbation method [20] as used for resonant EM cavities. A small blunt tip metallic needle of 300 μm outer diameter was mounted on an x/y -linear stage (VT80 150-2SM, PI miCos GmbH, Germany) to raster the resonator approximately 300 μm above its surface. The resonance frequency of the resonator is perturbed by the conducting tip by an amount depending upon the local electric and magnetic fields, which is therefore a measure of the field strength at the position of the tip [20]. The electric field strength in this region is related to the frequency shift by $|E|^2 \propto 1 - (\omega/\omega_0)$, where ω and ω_0 are the perturbed and unperturbed frequencies, respectively. For the measurement the linear stages and a network analyzer (N5224A, Agilent, USA) were controlled by a personal computer which also stored the x/y -coordinates as well as the corresponding resonance frequency data. Fig. 7 compares the simulated and measured electric field distributions side by side. The simulated field distribution shows the absolute value of the z -component E_z of the electric field at a height of 300 μm above the resonator surface and does not include the perturbation of the metallic tip. As the simulation confirms, this mode corresponds to the respective fundamental mode as depicted in Fig. 2. We note that the simulated electric field patterns ($|E|$ and $|E_z|$) of the second eigenmode ($f_{2\text{nd}} = 13.32$ GHz) appear almost similar when compared to the field distribution $|E_z|$ of the fundamental mode ($f_{1\text{st}} = 9.42$ GHz) and must not be confused.

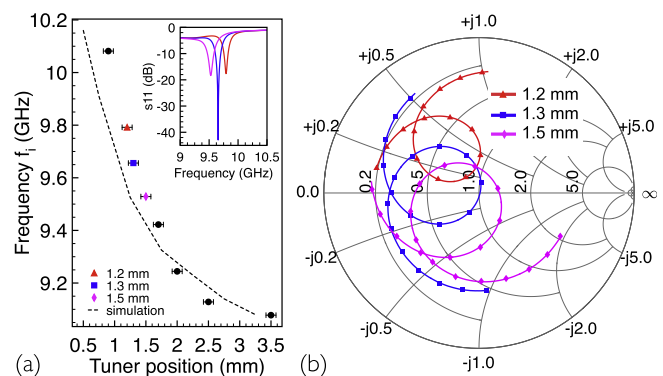


Fig. 6. (a) Measured (data points) and simulated (dashed line) shift of resonance frequencies f_i for different distances between the resonator surface and the copper tuning plate. The inset shows the measured spectra of the reflection coefficient S_{11} that correspond to the color-coded tuner positions. Error bars correspond to the standard error of the mean $\alpha = 0.1$ mm. (b) Smith chart representation for the measured S_{11} data at tuner positions 1.2 mm, 1.3 mm and 1.5 mm.

Table 2

Summarised data based on measurements presented in Fig. 6. Coupling factors κ were determined from the Q -circles plotted in a Smith chart (see Section 5 for details).

Tuner position	(mm)	1.2	1.3	1.5
f_i	(GHz)	9.79	9.66	9.53
Q_L	(-)	74	58	44
Q_0	(-)	106	93	78
κ	(-)	0.44	0.60	0.78

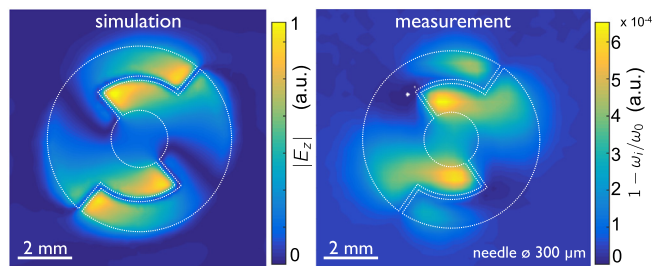


Fig. 7. (left) Simulated electric field distribution $|E_z|$ plotted in a parallel plane 300 μm above the resonator surface. (right) Measured field distribution as a function of $1 - \omega/\omega_0$. The measurement probe was approximately 300 μm positioned above the resonator surface. White dashed lines indicate the outline of the resonator.

4.2. EPR experiments

Electron paramagnetic resonance measurements were carried out using an X-band continuous-wave spectrometer (EMX, Bruker, Germany), with a tuneable MW frequency bridge (ER041MR) from 9 GHz to 10 GHz. The resonators were placed into the PMMA holder and the microstrip line coupling structure was connected to the spectrometer by a low-loss coaxial cable. The assembly was centred firmly between the poles of the EPR magnet to minimize vibrations during the measurements. The magnetic field generated by the custom-made modulation coil was calibrated by measuring a LiF crystal doped with Li particles of known g -factor of 2.00229 (as formed by neutron irradiation, LiF:Li) and a narrow line shape of 0.01 mT [21]. To load solid-state samples into the resonator, a hole was introduced to the top polyimide layer of the chip. For the calibration a modulation frequency of 50 kHz was used. In order to avoid any overmodulation, the dependency of the peak-to-peak linewidth ΔB_{pp} with respect to the modulation voltage was investigated to ensure $\Delta B_{pp} \leq 0.01$ mT. Fig. 8(a) shows the resulting LiF:Li spectra.

To estimate the limit of detection (LOD) for radical solutions, a concentration series was carried out (see Fig. 8(b)). It indicates that a 10 μM of S-(1-oxyl-2,2,5,5-tetramethyl-2,5-dihydro-1H-pyrrol-3-yl) methyl methanesulfonothioate (MTSL) in dimethyl sulfoxide (DMSO) is still detectable under our measurement conditions. The EPR spectra are well resolved and plausible, but also show an artefact becoming prominent at sufficient signal averaging and low MTSL concentrations. We attribute this background signal to paramagnetic species in the polymer chip materials. We would like to note, that similar measurements were carried out also with an aqueous sample. No significant changes in Q factor were observed during the EPR experiment. DMSO was chosen as a solvent due to higher solubility of MTSL. The minimal concentration detection limit c_{\min} for our resonator was determined from the signal-to-noise ratio (SNR) of the 1 mM MTSL sample. The noise level is given by the standard deviation of the baseline σ_{noise} , and the peak-to-peak signal level S_{pp} is the average over the three nitrogen hyperfine peaks, leading to an $\text{SNR} = S_{pp}/\sigma_{\text{noise}} \approx 243$. By taking into account the three isotropic hyperfine transitions of MTSL in DMSO

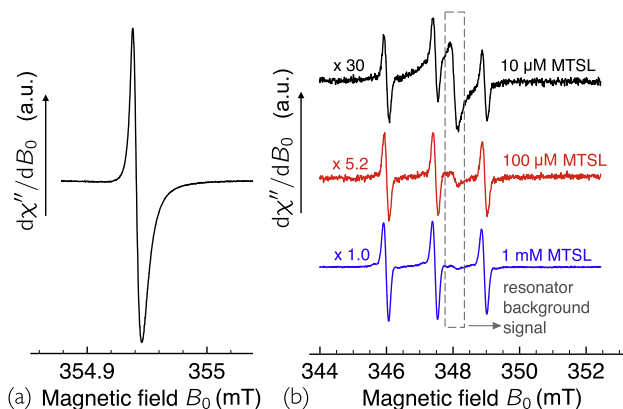


Fig. 8. (a) Measured EPR single-scan signal from a LiF:Li crystal at room temperature (RT). (experimental parameters: MW frequency $f_{\text{MW}} = 9.947$ GHz, MW power $P = 2$ mW, scan-rate 30 $\mu\text{T s}^{-1}$, filter constant $\tau_c = 5.12$ ms, modulation frequency $f_m = 50$ kHz with an amplitude of $B_m = 0.01$ mT) (b) Measured EPR spectra of a concentration series of MTSL dissolved in DMSO, recorded at RT. The (blue, red, black) curves correspond to MTSL concentrations of 1 mM after a single scan, 100 μM after a single scan, and 10 μM after 25 scans. (experimental parameters: $f_{\text{MW}} = 9.862$ GHz, $P = 6.3$ mW, scan-rate 238 $\mu\text{T s}^{-1}$, $\tau_c = 10.2$ ms, $f_m = 50$ kHz, $B_m = 0.14$ mT). (For interpretation of the references to colour in this figure legend, the reader is referred to the web version of this article.)

solution and three times σ_{noise} , the minimal concentration detection limit reads $c_{\min} = 1$ mM/SNR ≈ 4.1 μM for a single transition. Under given experimental conditions (equivalent noise bandwidth of $\Delta f_{\text{noise}} = 1/(4\tau_c) \approx 25$ Hz, average peak-to-peak linewidth of $\text{LW}_{pp} \approx 1.6$ G and resonator volume of $V_r \approx 2$ μL), the upper limit for the LOD for the resonator can be calculated as

$$\text{LOD} = \frac{c_{\min} V_r N_A}{\Delta f_{\text{noise}}^2 \text{LW}_{pp}} \cdot \eta \approx 6.2 \cdot 10^{11} \frac{\text{spins}}{\text{Hz}^{1/2} \text{G}} \cdot \eta, \quad (1)$$

where $N_A = 6.022140857 \cdot 10^{23} \text{ mol}^{-1}$ is the Avogadro constant.

To experimentally determine the MW conversion factor A_{exp} , preliminary transient EPR experiments were carried out on a p-terphenyl crystal hosting pentacene at a concentration of 1000 ppm [22]. A typical crystal was of cube like shape of approximately 0.8 mm edge length. The MW conversion efficiency can be calculated directly from the transient nutation frequency ω_n [23] of the light-induced pentacene triplet state. The pentacene inside the crystal was excited using a laser light source (Spectra Physics GCR 190-10 Nd:Yag) and an optical parametric oscillator (Opta BBO-355-Visible/IR) at a wavelength of 532 nm and a pulse rate of 10 Hz. The laser light was coupled into a glass fibre, which was guided through the frequency tuning screw of the resonator and positioned directly above the crystal, in the middle of the resonator. Transient nutation experiments were carried out on a Bruker ESP-300E spectrometer with a Bruker ER046 MRT MW bridge. The data was recorded with an oscilloscope (LeCroy 9354A, 500 MHz). Fig. 9(a) shows the transient nutation for two different MW powers at the maximum emissive resonance of pentacene.

The transient nutation is mainly dominated by a zero-order Bessel function J_0 multiplied by an exponential decay function due to T_2 [22,23]. To obtain the transient nutation frequency, the nutation plot was Fourier transformed. Before FFT, the starting point was set to the first maximum of oscillation, and also a zero filling and a Hamming window was applied. Fig. 9(b) shows the dependency of the nutation frequency for different square root MW powers. Using the equation $\omega_n = \gamma_e B_1 2^{1/2}$, and assuming for the g -factor a value of 2 for pentacene, the nutation frequency can be transformed into B_1 -field strength. This leads to a MW conversion efficiency of $A_{\text{exp}} = 0.12 \text{ mT W}^{-1/2}$.

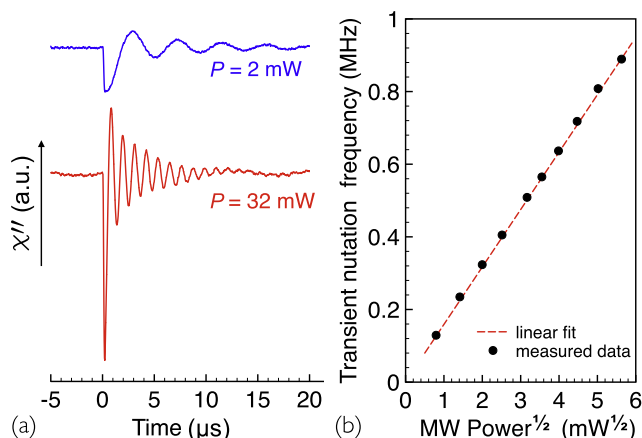


Fig. 9. (a) Measured light-induced transient EPR nutations of pentacene in p-terphenyl at $B_0 = 360$ mT, 9.37072 GHz, with a laser-pulse energy of 2 mJ. (b) Nutation frequency vs. square root of the MW power P . The linear slope of 0.158 MHz/ $\text{mW}^{-1/2}$ is directly derived from the measured data and corresponds to a MW conversion efficiency of $A_{\text{exp}} = 0.12$ mT $\text{W}^{-1/2}$ (see text).

5. Discussion and conclusion

We introduced a MW resonator co-integrated with a microfluidic chip and fabricated in a batch process that combines surface micromachining techniques with a simple lamination step, and that allows rapid fabrication of multiple resonators within 3 h. The fluidic channels allow precise delivery and positioning of sub-microliter sample volumina for EPR measurements. The structures can be defined by the layout of the mid polymer layer and are therefore adjustable in a flexible way. The typical sample volume within the active region of the proposed resonator is around $1 \mu\text{L}$.

The EM performance of the resonator was characterised by FEM simulations, RF as well as EPR measurements. The simulation results for the dependency of f_i on the design parameter θ (see Fig. 5) are in excellent agreement with the measured data, for a given structure within 2%. Linear fits to the curves show slopes of approximately -49 MHz/ $^\circ$ for the calculated and -46 MHz/ $^\circ$ for the measured curve, respectively. Therefore, multiple resonator chips of identical outer diameter covering different frequency ranges can be fabricated in a single process run. On average, the simulated and measured loaded quality factors Q_L were found to be approximately 65 and 56, respectively. Minor deviations between experimental and simulated results were mainly attributed to inadequate material properties at high frequencies, additional external loss factors, as well as surface roughness. Also, the simulation model did not account for the co-axial cable to microstrip line transition, which may have introduced minor frequency offsets.

As for the determination of the unloaded quality Q_0 and coupling factors κ (see Table 2), we note that the Q-circles for the fabricated resonators, shown in Fig. 6(b), are detached from the perimeter of the Smith chart, indicating coupling losses, probably due to the high reactance of the coupling structure. We therefore redefined the perimeter value of the Smith chart and normalised the Q-circle diameters as described by Kajfez [24] to extract the coupling factors κ . The copper tuning plate allows both continuous frequency tuning as well as impedance matching. Critical coupling was achieved as indicated by coupling factors κ of approximately 1 (see Table 2). The resonance frequency could only be increased, which can be explained by the perturbational principle for the case of inward perturbations at points of large magnetic fields [25]. The achievable shift in resonance frequency $|\Delta f_0|$ is about 1 GHz over the whole travel range of the tuner. The tuner can be further

optimised to decrease radiation loss and to increase the quality factor of the resonators, as suggested by Narkowicz and Suter [26].

An EPR spectrum of a LiF:Li standard was successfully measured to calibrate the custom-made modulation coil. Further CW measurements were carried out using this calibration curve. By using a known concentration of MTSL dissolved in DMSO and considering a filling factor of $\eta \approx 0.6$, the LOD of the resonator could be estimated to be around $3.7 \cdot 10^{11}$ spins $\cdot \text{Hz}^{-1/2} \text{G}^{-1}$ in solution for a single EPR transition.

The simulation study reveals a calculated value for A_{cal} of 0.39 mT $\text{W}^{-1/2}$ and geometrically well separated magnetic and electric field maxima. The minimum of the simulated electric field intensity $|E_{\text{min}}|$ of 5 kV m^{-1} is located in the centre of the resonator. We determined an average electric field intensity over the inner diameter of 2 mm of approximately 13 kV m^{-1} . For comparison, Narkowicz et al. [11] presented simulations for a R-shaped PMR with a loop diameter of $50 \mu\text{m}$ featuring an average electric field intensity across the sample of approximately 600 kV m^{-1} . Twig et al. [27] published electric field distributions for an Ω -shaped surface resonator with a loop diameter of $400 \mu\text{m}$ featuring an average electric field intensity across the sample of approximately 243 kV m^{-1} . These numbers for the electric field intensities (input power $P = 1$ W) put our results in context. However, we note that the values A_{cal} for above mentioned resonators are much higher due to their small size.

First measurements with transient EPR on the light-induced triplet state of pentacene in p-terphenyl crystals show a good possibility to determine A at low MW powers (see Fig. 9). The MW conversion efficiency obtained was 0.12 mT $\text{W}^{-1/2}$. This value was calculated with a g -factor of 2, and assuming a transition moment of $2^{1/2}$ for the allowed triplet transitions in the high-field limit. The discrepancy of a factor of three (i.e., 0.12 mT $\text{W}^{-1/2}$ instead of 0.39 mT $\text{W}^{-1/2}$) between the calculated and experimentally determined MW conversion factor might be due to diffusion of sample solvent into high electric field regions of the resonator, as well as an incorrectly centred pentacene crystal.

Owing to the material composition, aggressive solvents should be avoided as they tend to dissolve the polymer material. Also, the EPR spectra shown in Fig. 8(b) reveal a fixed background signal originating from the polymer chip itself. Therefore, next-generation resonator chips will be made from glass and other EPR compatible materials. A suitable process was published by Spengler et al. [28,29], who developed a compatible process to fabricate sample inserts for nuclear magnetic resonance experiments based on glass, increasing chemical as well as mechanical robustness substantially. Also, high permittivity substrates like ceramics or sapphire can further decrease the resonator feature size, which is roughly proportional to $\epsilon^{-1/2}$ and hence increase A .

Further improvements for the simulation procedures might consider the trade-off between minimal active resistance of the structure, and maximum magnetic field values, as well as the increase in MW efficiency versus ring diameter.

Acknowledgements

We acknowledge the group of Prof. Dr. L.M. Reindl at the University of Freiburg as well as Dr. G. Gantenbein, Dr. S. Soldatov and V. Ramopoulos from the Institute for Pulsed Power and Microwave Technology (IHM) at Karlsruhe Institute of Technology for providing technical support and access to their MW metrology equipment. We thank Prof. Dr.-Ing. U. Wallrabe at University of Freiburg for access to her laboratories. We also thank Katharina Koeler and Sarah Mueller for their diligent work concerning this project. SZK, NS, MVM, NM and JGK gratefully acknowledge funding through the NMCEL project of the European Research Council

under contact No. 290586. ES and SW were supported by the Deutsche Forschungsgemeinschaft (DFG Priority Program 1601).

Appendix A. Supplementary data

Supplementary data associated with this article can be found, in the online version, at <http://dx.doi.org/10.1016/j.jmr.2016.07.008>.

References

- [1] B. Johansson, A stripline resonator for ESR, *Rev. Sci. Instrum.* 45 (11) (1974) 1445, <http://dx.doi.org/10.1063/1.1686524>. <<http://scitation.aip.org/content/aip/journal/rsi/45/11/10.1063/1.1686524>>.
- [2] H. Mahdjour, W.G. Clark, K. Baberschke, High-sensitivity broadband microwave spectroscopy with small nonresonant coils, *Rev. Sci. Instrum.* 57 (6) (1986) 1100, <http://dx.doi.org/10.1063/1.1138664>. <<http://link.aip.org/link/RISNAK/v57/i6/p1100/s1&Agg=doi>>.
- [3] R. Narkowicz, D. Suter, R. Stonies, Planar microresonators for EPR experiments, *J. Magn. Reson.* 175 (2) (2005) 275–284, <http://dx.doi.org/10.1016/j.jmr.2005.04.014>. <<http://linkinghub.elsevier.com/retrieve/pii/S1090780705001448>>.
- [4] T. Yalcin, G. Boero, Single-chip detector for electron spin resonance spectroscopy, *Rev. Sci. Instrum.* 79 (9) (2008), <http://dx.doi.org/10.1063/1.2969657>. <<http://link.aip.org/link/RISNAK/v79/i9/p094105/s1&Agg=doi>>.
- [5] Y. Twig, E. Dikarov, W.D. Hutchison, A. Blank, Note: high sensitivity pulsed electron spin resonance spectroscopy with induction detection, *Rev. Sci. Instrum.* 82 (7) (2011) 076105, <http://dx.doi.org/10.1063/1.3611003>. <<http://link.aip.org/link/RISNAK/v82/i7/p076105/s1&Agg=doi>>.
- [6] J. Anders, A. Angerhofer, G. Boero, K-band single-chip electron spin resonance detector, *J. Magn. Reson.* 217 (2012) 19–26, <http://dx.doi.org/10.1016/j.jmr.2012.02.003>. <<http://linkinghub.elsevier.com/retrieve/pii/S1090780712000602>>.
- [7] A. Blank, E. Dikarov, R. Shklyar, Y. Twig, Induction-detection electron spin resonance with sensitivity of 1000 spins: En route to scalable quantum computations, *Phys. Lett. A* 377 (31–33) (2013) 1937–1942, <http://dx.doi.org/10.1016/j.physleta.2013.05.025>. <<http://linkinghub.elsevier.com/retrieve/pii/S03759601130004957>>.
- [8] G. Gualco, J. Anders, A. Sienkiewicz, S. Alberti, L. Forró, G. Boero, Cryogenic single-chip electron spin resonance detector, *J. Magn. Reson.* 247 (2014) 96–103, <http://dx.doi.org/10.1016/j.jmr.2014.08.013>. <<http://linkinghub.elsevier.com/retrieve/pii/S109078071400233X>>.
- [9] A. Bienfait, J.J. Pla, Y. Kubo, M. Stern, X. Zhou, C.C. Lo, C.D. Weis, T. Schenkel, M. L.W. Thewalt, D. Vion, D. Esteve, B. Julsgaard, K. Mølmer, J.J.L. Morton, P. Bertet, Reaching the quantum limit of sensitivity in electron spin resonance, *Nat. Nanotechnol.* 11 (3) (2015) 253–257, <http://dx.doi.org/10.1038/nnano.2015.282>. <<http://www.nature.com/doi/10.1038/nnano.2015.282>>.
- [10] J.P. Campbell, J.T. Ryan, P.R. Shrestha, Z. Liu, C. Vaz, J.-H. Kim, V. Georgiou, K.P. Cheung, Electron spin resonance scanning probe spectroscopy for ultrasensitive biochemical studies, *Anal. Chem.* (Washington) 87 (9) (2015) 4910–4916, <http://dx.doi.org/10.1021/acs.analchem.5b00487>. <<http://pubs.acs.org/doi/abs/10.1021/acs.analchem.5b00487>>.
- [11] R. Narkowicz, D. Suter, I. Niemeyer, Scaling of sensitivity and efficiency in planar microresonators for electron spin resonance, *Rev. Sci. Instrum.* 79 (8) (2008), <http://dx.doi.org/10.1063/1.2964926>. <<http://scitation.aip.org/content/aip/journal/rsi/79/8/10.1063/1.2964926>>. 084702–084702.
- [12] Y.S. Yap, H. Yamamoto, Y. Tabuchi, M. Negoro, A. Kagawa, M. Kitagawa, Strongly driven electron spins using a Ku band stripline electron paramagnetic resonance resonator, *J. Magn. Reson.* 232 (2013) 62–67, <http://dx.doi.org/10.1016/j.jmr.2013.04.015>. <<http://linkinghub.elsevier.com/retrieve/pii/S1090780713001080>>.
- [13] W.J. Wallace, R.H. Silsbee, Microstrip resonators for electron-spin resonance, *Rev. Sci. Instrum.* 62 (7) (1991) 1754, <http://dx.doi.org/10.1063/1.1142418>. <<http://scitation.aip.org/content/aip/journal/rsi/62/7/10.1063/1.1142418>>.
- [14] A.C. Torrezan, T.P.M. Alegre, G. Medeiros-Ribeiro, Microstrip resonators for electron paramagnetic resonance experiments, *Rev. Sci. Instrum.* 80 (7) (2009) 075111, <http://dx.doi.org/10.1063/1.3186054>. <<http://scitation.aip.org/content/aip/journal/rsi/80/7/10.1063/1.3186054>>.
- [15] Y. Twig, E. Dikarov, A. Blank, Ultra miniature resonators for electron spin resonance: sensitivity analysis, design and construction methods, and potential applications, *Mol. Phys.* 111 (18–19) (2013) 2674–2682, <http://dx.doi.org/10.1080/00268976.2012.762463>. <<http://www.tandfonline.com/doi/abs/10.1080/00268976.2012.762463>>.
- [16] J.B. Pendry, A.J. Holden, D.J. Robbins, W.J. Stewart, Magnetism from conductors and enhanced nonlinear phenomena, *IEEE Trans. Microw. Theory Tech.* 47 (11) (1999) 2075–2084, <http://dx.doi.org/10.1109/22.798002>. <<http://ieeexplore.ieee.org/lpdocs/epic03/wrapper.htm?arnumber=798002>>.
- [17] R. Marques, F. Mesa, J. Martel, F. Medina, Comparative analysis of edge- and broadside-coupled split ring resonators for metamaterial design – theory and experiments, *IEEE Trans. Antennas Propag.* 51 (10) (2003) 2572–2581, <http://dx.doi.org/10.1109/TAP.2003.817562>. <<http://ieeexplore.ieee.org/lpdocs/epic03/wrapper.htm?arnumber=1236074>>.
- [18] T. Li, H. Liu, S. Wang, J. Cao, Z. Zhu, Z. Dong, S. Zhu, X. Zhang, Suppression of radiation loss by hybridization effect in two coupled split-ring resonators, *Phys. Rev. B* 80 (11) (2009) 115113, <http://dx.doi.org/10.1103/PhysRevB.80.115113>. <<http://link.aps.org/doi/10.1103/PhysRevB.80.115113>>.
- [19] I.J. Bahl, *Lumped Elements for RF and Microwave Circuits*, Artech House, 2003. <<http://cds.cern.ch/record/2066090>>.
- [20] L.C. Maier, J.C. Slater, Field strength measurements in resonant cavities, *J. Appl. Phys.* 23 (1) (1952) 68, <http://dx.doi.org/10.1063/1.1701980>. <<http://scitation.aip.org/content/aip/journal/jap/23/1/10.1063/1.1701980>>.
- [21] A. Stesmans, G. Van Gorp, Improved measurement of the g factor of conduction electrons in Li particles embedded in LiF:Li, *Phys. Lett. A* 139 (1–2) (1989) 95–98, [http://dx.doi.org/10.1016/0375-9601\(89\)90616-6](http://dx.doi.org/10.1016/0375-9601(89)90616-6). <<http://linkinghub.elsevier.com/retrieve/pii/S0375960189906166>>.
- [22] J.H. Moore, N.D. Spencer, *Encyclopedia of Chemical Physics and Physical Chemistry – 3 Volume Set*, Institute of Physics Publishing, 2001.
- [23] A.J. Hoff, *Advanced EPR, Applications in Biology and Biochemistry*, Elsevier Science, 2012.
- [24] D. Kajfež, Q-Factor, in: onlinelibrary.wiley.com, John Wiley & Sons, Inc., Hoboken, NJ, USA, 2005, pp. 3937–3949. doi:<http://dx.doi.org/10.1002/0471654507.eme333>.
- [25] R.F. Harrington, *Time-Harmonic Electromagnetic Fields*, Wiley-IEEE Press, 2001, <http://dx.doi.org/10.1109/9780470546710>.
- [26] R. Narkowicz, D. Suter, Tuner and radiation shield for planar electron paramagnetic resonance microresonators, *Rev. Sci. Instrum.* 86 (2) (2015) 024701, <http://dx.doi.org/10.1063/1.4906898>. <<http://scitation.aip.org/content/aip/journal/rsi/86/2/10.1063/1.4906898>>.
- [27] Y. Twig, E. Suhovoy, A. Blank, Sensitive surface loop-gap microresonators for electron spin resonance, *Rev. Sci. Instrum.* 81 (10) (2010) 104703, <http://dx.doi.org/10.1063/1.3488365>. <<http://scitation.aip.org/content/aip/journal/rsi/81/10/10.1063/1.3488365>>.
- [28] N. Spengler, A. Moazenzadeh, R.C. Meier, V. Badilita, J.G. Korvink, U. Wallrabe, Micro-fabricated Helmholtz coil featuring disposable microfluidic sample inserts for applications in nuclear magnetic resonance, *J. Micromech. Microeng.* 24 (3) (2014) 034004, <http://dx.doi.org/10.1088/0960-1317/24/3/034004>. <<http://stacks.iop.org/0960-1317/24/i=3/a=034004?key=crossref.d6de15dca6f5cbe27ec4407bb094d689>>.
- [29] N. Spengler, J. Höfflin, A. Moazenzadeh, D. Mager, N. MacKinnon, V. Badilita, U. Wallrabe, J.G. Korvink, Heteronuclear micro-helmholtz coil facilitates μm -range spatial and sub-Hz spectral resolution NMR of nL-volume samples on customisable microfluidic chips, *PLOS ONE* 11 (1) (2016) e0146384, <http://dx.doi.org/10.1371/journal.pone.0146384.s003>. <<http://dx.plos.org/10.1371/journal.pone.0146384.s003>>.